Asian Journal of Chemistry; Vol. 38, No. 7 (2026), 1713-1724
ASIAN JOURNAL OF CHEMISTRY
https://doi.org/10.14233/ajchem.2026.35981

Synthesis of Bi^{3+} Co-doped ZnO:Eu^{3+} Nanophosphors: Enhanced Photoluminescence and Photocatalytic Activity

KANGJAM MISHESHWORI DEVI, HENAM SYLVIA DEVI and R.K. LONDON SINGH*,

Department of Chemistry, Dhanamanjuri University, Imphal-795001, India

*Corresponding author: E-mail: london_ningthemcha@yahoo.com

Received: 12 March 2026 *Accepted*: 14 May 2026 *Published online*: 3 July 2026 AJC-22397

Pure ZnO, Eu^{3+} (3 at.%) doped ZnO, Bi^{3+} (3 at.%) doped ZnO and Bi^{3+} (1, 3 at.%) co-doped Zn_xO:Eu^{3+} (3 at.%) have been synthesised through the co-precipitation method at 25 ºC, with ethylene glycol as a capping agent. The crystallite sizes, estimated using the Scherrer equation, ranged from 8-11 nm and were consistent with TEM observations. FTIR analysis confirmed the presence of characteristic Zn–O, O–H and CH_2 stretching vibrations associated with ethylene glycol. Furthermore, incorporation of dopants into the ZnO lattice led to a reduction in the optical band gap from 3.07 to 2.85 eV, as determined from Tauc plot analysis, indicating enhanced visible-light absorption. Sensitised Bi^{3+} (1, 3 at.%) co-doped Zn_xO:Eu^{3+} (3 at.%) samples enhanced its absorption peaks at 464 nm ($^7F_0 \rightarrow {}^5D_2$) and 394 nm ($^7F_0 \rightarrow {}^5L_6$) of Eu^{3+} transition. The photoluminescence emission intensity of Eu^{3+}, observed at 615 nm ($^5D_0 \rightarrow {}^7F_J$, where J = 0, 1, 2, 3 and 4), is enhanced through Bi^{3+} doping than under direct Eu^{3+} excitation. Bi^{3+} (3 at.%) co-doped $Zn_{0.94}O$:$Eu^{3+}_{0.03}$ has demonstrated promising photocatalytic activity in the degradation of crystal violet dye under UV exposure.

Keywords: Co-precipitation, Room temperature, Nanoparticles, Luminescence, Photodegradation.

INTRODUCTION

Recently, material science has emphasised the greater impact of wide-bandgap semiconductor nanomaterials in the advancement of technology and optoelectronics. Semiconductor nanomaterials, such as indium tin oxide (ITO), ZnS, ZnO, TiO_2, ZnSe, CdSe, *etc*. displayed superior optical characteristics [1]. Among these, ZnO is a promising material among researchers, it has an optical bandgap of ~3.37 eV and large exciton binding energy ~60 meV [2]. Owing to its low toxicity and cost effectiveness, ZnO has recently attracted significant attention due to its superior electrochemical durability and optimised electrocatalytic properties. ZnO when doped with different metals and rare earth (RE^{3+}) elements exhibits diverse properties including high transparency, tunable conductivity, electronic modifications, insulating states, piezoelectricity, enhanced luminescence, antibacterial properties, photocatalytic efficiency, drug delivery capability, gas sensors and batteries by altering its structure and material characteristics [3-8]. The ionic radius of the dopants significantly influences its ability to incorporate into the crystal lattice by causing structural distortion.

Doping ZnO with Bi, a post-transition metal from group 15, contributes to superior magnetic properties, hybrid solar cells, optical behaviour, structural characteristics, by improving crystallinity of the material and maintains stability even at elevated temperatures [9,10]. Ntwaeaborwa *et al*. [11] state that the incorporation of activator Eu^{3+} into ZnO has a significance influence on both structural and luminescence due to the *f-f* transition. Photoluminescence efficiency can be further optimised by introducing a sensitizer (such as Ce^{3+}, Bi^{3+}, Tb^{3+}, Gd^{3+}) as a co-dopant in ZnO. Bi^{3+} co-doped Eu^{3+}: ZnO-B_2O_3 enhance the luminescence of ZnO, which is found to be shifting towards the longer wavelength and leading to higher brightness and a broader emission spectrum compared to single doped ZnO [12]. Yaba *et al*. [13] reported that energy transfer observed from the sensitizer Bi^{3+} to the activator Eu^{3+}, when the Bi^{3+} (at.%) increase the intensity also found increases; however, as the Bi^{3+} concentration reach 11 at.%, the emission intensity decreases, which can be due to the formation of Bi^{3+} cluster leads to luminescence quenching.

Doping and co-doping system into ZnO improve the separations of charge carrier and electron-hole and alters the electronic structure leading to improved photocatalytic perfor-

mance under UV or visible light [14,15]. Rhodamine B, methyl orange and picric acid dyes were discussed by using ZnO:Eu^{3+} catalyst under UV light source (125 W Hg vapour lamp) [16], while Cu^{2+}/Bi^{3+} doped ZnO@cotton fabric were used in the degradation of methylene blue (MB) under a visible light (100 W halogen lamp) [17].

Several studies have investigated the individual doping of RE elements and metals into ZnO by different methods of synthesis, such as solvothermal, co-precipitation, combustion, hydrothermal method, facile and silar [18-20]. Previous studies on Eu^{3+}/Bi^{3+} co-doped materials have mainly emphasised on luminescent host lattices such as XWO_4 (X = Sr, Ba, Ca), YVO_4, LaF_3, YPO_4, Y_2O_3, $GdPO_4$ and Y_2O_3, in which Bi^{3+} ions generally act as efficient sensitizers to increase Eu^{3+} emission [21-24]. However, most of these synthesis approaches involve high temperatures and post-annealing treatments, which are not cost-effective or economical. Reports on ZnO as the host matrix co-doped with Bi^{3+} and Eu^{3+} ions are limited.

This study reports the synthesis of pure ZnO, $Zn_{0.97}O$:$Eu^{3+}_{0.03}$, $Zn_{0.97}O$:$Bi^{3+}_{0.03}$ and Bi^{3+} (1, 3 at.%) co-doped Zn_xO:$Eu^{3+}_{0.03}$, using a co-precipitation technique performed at low temperature, thereby reducing energy consumption. The novelty of this work highlights the role of Bi^{3+} co-doping in tuning the optical emission of Eu^{3+} and its impact on photocatalytic degradation efficiency of crystal violet (CV) dye supported by reactive oxygen species analysis. The effectiveness of the prepared samples as photocatalysts was investigated by observing the degradation of CV under exposure to UV light.

EXPERIMENTAL

High-purity, analytical grade chemicals were used throughout the synthesis process without any additional purification. Zinc acetate dihydrate ($Zn(CH_3COO)_2{\cdot}2H_2O$, 99.99%, Sigma-Aldrich), bismuth nitrate pentahydrate ($Bi(NO_3)_3{\cdot}5H_2O$, 99.99%, Sigma-Aldrich), europium nitrate ($Eu(NO_3)_3$, 99.99% , Sigma-Aldrich) were employed as Zn^{2+}, Bi^{3+} and Eu^{3+} precursors and sodium hydroxide (97%, Emplura, India) as a precipitating agent. Mono-ethylene glycol (99%, SRL, India) was used as both the solvent and capping agent.

Synthesis of ZnO and $Zn_{0.94}O$:$Eu^{3+}_{0.03}$:$Bi^{3+}_{0.03}$ nanoparticles: $Zn(CH_3COO)_2{\cdot}2H_2O$ (1 g) was dissolved in 25 mL of ethylene glycol (EG) in a beaker and stirred for 10 min. Under continuous stirring, NaOH (1 M) was added dropwise to the reaction mixture to adjust the pH of the medium at 8. The resulting solution was then vigorously stirred for 30 min to ensure homogeneous mixing. The obtained white colloidal mixture was left undisturbed overnight, after which the solid product was isolated by centrifugation (10,000 rpm). For purity, the sample was washed with distilled water (four times) and finally with ethanol. Subsequently, the nanoparticles (NPs) were dried in an oven for 8 h at 65 ºC. For a typical synthesis of $Zn_{0.94}O$:$Eu^{3+}_{0.03}$:$Bi^{3+}_{0.03}$, 0.0648 g of $Eu(NO_3)_3$ was added into the $Zn(CH_3COO)_2{\cdot}2H_2O$ solution and continued to stirred for 10 min and followed by the addition of $Bi(NO_3)_3{\cdot}5H_2O$ (0.0708 g). The reaction medium was adjusted to pH 8 by adding NaOH (1 M) slowly, followed by constant stirring for 30 min. Other samples were synthesised similarly by measuring out the required stoichiometric amounts of precursors.

Characterisation: The powder X-ray diffraction (PXRD) peaks were measured using an XPERT-PRO X-ray (PANalytical BV) diffractometer with Cu*K*α (λ = 1.506 Å) radiation. The elemental composition of both pristine and composite materials was investigated using energy dispersive X-ray analysis (EDAX), as measured by METEK spectrophotometer. Fourier transform infrared (FTIR) spectra were measured using a Shimadzu-RAffinity-IS instrument. The optical analysis was derived from a UV-Vis spectrophotometer (Shimadzu Corp., model-82420) by scanning in the range of λ = 200-800 nm. Photoluminescence (PL) spectra were recorded using a Horiba-FluroMax-4CP spectrofluorometer by exciting with a 150 W Xenon lamp at room temperature. Transmission electron microscope (TEM) images of $Zn_{0.97}O$:$Bi^{3+}_{0.03}$ NPs were acquired by using a JEOL JEM-1400 microscope operating at HV = 200 kV.

Catalytic activity: The photocatalytic response of the catalyst was tested by monitoring the photodegradation of CV dye under UV irradiation (λ = 365 nm). Each sample (5 mg) was dispersed in 30 mL of distilled water and sonicated for 25 min. Thereafter, aqueous CV solution (3.1×10^{-5} M) was added to the catalyst solution, then the catalyst-dye mixture was maintained under dark conditions for 30 min with bath sonication to established adsorption-desorption equilibrium and prior to irradiation, the initial (0 min) UV absorbance was measured. The absorption spectra of the catalyst-dye mixture were measured every 20 min after exposure to the irradiation source. The samples were filtered using syringe filter (0.45 μm, PTFE) prior to analysis.

For the recyclability study, the $Zn_{0.94}O$:$Eu^{3+}_{0.03}$:$Bi^{3+}_{0.03}$ catalyst was collected after each cycle by centrifugation, washed five times with double-distilled water followed by ethanol (once), then dried at 65 ºC for 8 h and reused for further photocatalytic reactions under UV irradiation.

Terephthalic acid photoluminescence test: A terephthalic acid (TA) probe solution of 3×10^{-5} M was prepared by dissolving terephthalic acid (5 mg) in 10 mL of 0.1 M NaOH solution. The catalyst suspension (2 mg in 5 mL) was mixed with probe solution and homogenised under continuous stirring for 30 min in the dark to achieve adsorption-desorption equilibrium. The suspension was then exposed to UV light (λ = 365 nm) and collected aliquots were filtered. The excitation wavelength was set at 315 nm and the emission peak at 425 nm of 2-hydroxy terephthalic acid (2-HTA) was monitor for hydroxyl radical (•OH) formation.

NBT spectrophotometric test: Nitro blue tetrazolium (NBT, 4 mg) was dissolved in 100 mL of ~7 pH buffer solution and magnetically stirred for 30 min at 37 ºC. Subsequently, 2 mg of catalyst was dispersed into the NBT solution under continuous stirring for 30 min at dark condition to obtain adsorption-desorption equilibrium. The catalyst-NBT suspension was then irradiated under UV (λ = 365 nm).

RESULTS AND DISCUSSION

PXRD analysis: The PXRD patterns of pristine ZnO, $Zn_{0.97}O$:$Eu^{3+}_{0.03}$, $Zn_{0.97}O$:$Bi^{3+}_{0.03}$ and Bi^{3+} (1, 3 at.%) co-doped Zn_xO:$Eu^{3+}_{0.03}$ (where x = 0.96, 0.94) NPs prepared at 25 ºC, are shown in Fig. 1a. All the patterns conform to the reference

hexagonal wurtzite structure of pure ZnO (JCPDS No. 36-1451, a = b = 3.2498 Å, c = 5.2066 Å, v = 47.62 $Å^3$) [25]. No other diffraction peaks for Eu and Bi metal or secondary peaks such as Bi_2O_3, Eu_2O_3 and EuO were observed in any of the samples except ZnO peaks, signifying that Eu^{3+} and Bi^{3+} ions have been incorporated into the interstitial site of the ZnO lattice. In Fig. 1b, In comparison with pure ZnO, the doped samples show diminished intensity and increased broadening of the characteristic diffraction peaks as the dopant concentration increases, which can be attributed to the generation of defects and lattice distortions within the ZnO crystal structure [16]. The incorporation of different ionic radii, Zn^{2+} (0.074 nm), Bi^{3+} (0.103 nm) and Eu^{3+} (0.095 nm) ions, results in a decrease in lattice parameters accompanied by a shift of the diffraction peak toward higher angles.

The crystallite size (d) of the samples was calculated from the most three intense peaks at 2θ values of 31.7º (100), 34.4º (002) and 36.2º (101) by using the Debye-Scherrer equation:

$$d_{hkl} = \frac{K\lambda}{\beta \cos\theta} \quad (1)$$

here, d = average crystallite size; k (0.94 for ZnO) represents a shape factor; λ (1.5406 Å) is the X-ray wavelength; θ denotes the diffraction angle; and β corresponds to the full width at half maximum (FWHM). The crystallinity of ZnO was found to improve with Eu^{3+} ion doping, likely due to the substitution of Zn^{2+} by Eu^{3+}, which has a larger ionic radius than the Zn^{2+} ion, causing greater lattice distortion when substituted into the ZnO structure [26]. This substitution may enhance the structural ordering within the crystal lattice. However, a reduction in crystallinity was observed upon doping and co-doping with Bi^{3+} ions. This decrease can be attributed to the substantially larger ionic radius of Bi^{3+} compared to Zn^{2+}, which introduces lattice strain, distorts the crystal structure and promotes structural disorder within the ZnO lattice [27]. The unit-cell volume and lattice parameter of the samples were calculated *via* UnitCellWin software by indexing the experimentally observed diffraction peaks of the hexagonal wurtzite ZnO structure. Table-1 shows the crystallite sizes (d), unit cell parameters and unit-cell volume of the prepared samples.

TEM analysis: TEM image of $Zn_{0.97}O:Bi^{3+}_{0.03}$ NPs (Fig. 2a) reveals a spherical morphology. The average particle diameter was determined using Image J software and was found to be ~8.709 ± 0.8 nm, which is validated by crystallite size derived from XRD analysis. A Gaussian fitting (using Origin) of the particle size distribution histogram is shown in Fig. 2b.

FTIR analysis: FTIR spectra of the pure ZnO, $Zn_{0.97}O:Eu^{3+}_{0.03}$, $Zn_{0.97}O:Bi^{3+}_{0.03}$ and $Zn_{0.94}O:Eu^{3+}_{0.03}:Bi^{3+}_{0.03}$ samples are shown in Fig. 3. The bands at 673 cm^{-1}, 411 cm^{-1} are due to stretching vibrations of Zn-O whereas, 875 cm^{-1} is due to stretching vibrations of O-Zn-O [28]. The absorption band observed between 1091-1041 cm^{-1} is due to the stretching

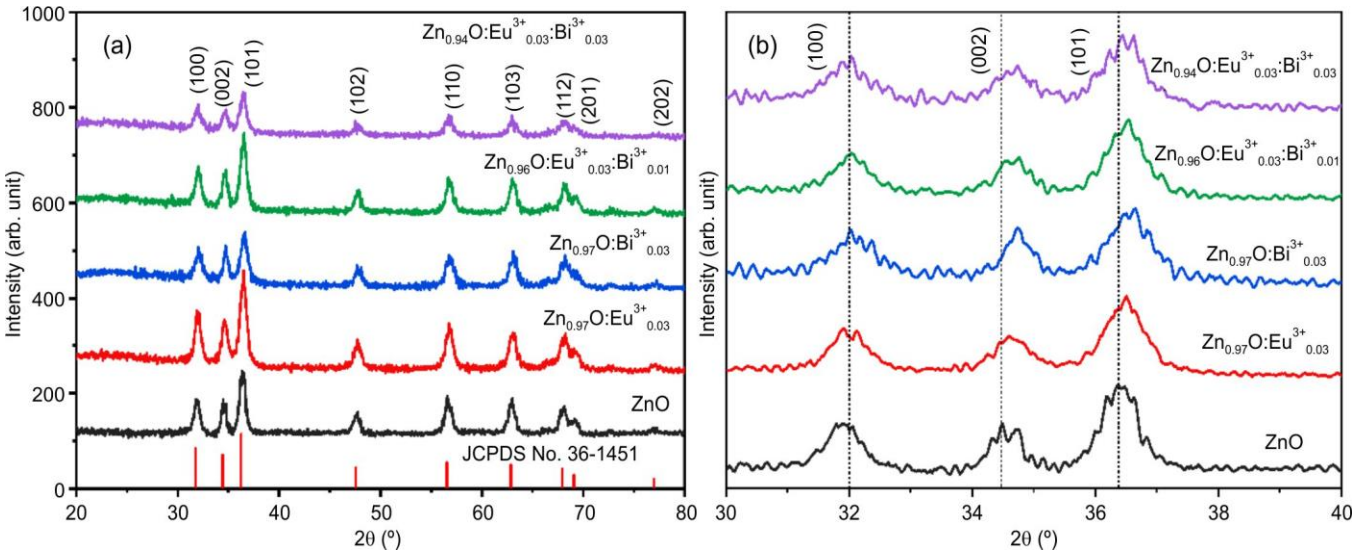

Fig. 1. (a) PXRD patterns of pure ZnO, $Zn_{0.97}O:Eu^{3+}_{0.03}$, $Zn_{0.97}O:Bi^{3+}_{0.03}$ and Bi^{3+} (1, 3 at.%) co-doped $Zn_xO:Eu^{3+}_{0.03}$; (b) shifting of the most significant diffraction peaks toward higher angles upon doping

TABLE-1
CRYSTALLITE SIZE (d), LATTICE CONSTANTS (a, c) AND CELL VOLUME (V) OF Bi^{3+} Co-doped ZnO:Eu^{3+} NANOPHOSPHORS

S. No.	Sample	Crystallite size, d (nm)	Lattice parameters		
			a (Å)	c (Å)	V ($Å^3$)
1	ZnO	9.21	3.23572	5.18887	47.3397
2	$Zn_{0.97}O:Eu^{3+}_{0.03}$	10.38	3.23894	5.19823	47.0637
3	$Zn_{0.97}O:Bi^{3+}_{0.03}$	8.83	3.23496	5.16801	46.8973
4	$Zn_{0.96}O:Eu^{3+}_{0.03}:Bi^{3+}_{0.01}$	9.82	3.24315	5.19503	47.1388
5	$Zn_{0.94}O:Eu^{3+}_{0.03}:Bi^{3+}_{0.03}$	8.73	3.23074	5.19503	47.3476
6	Reused NPs*	10.67	3.23780	5.18101	47.0375

*Based on Fig. 15.

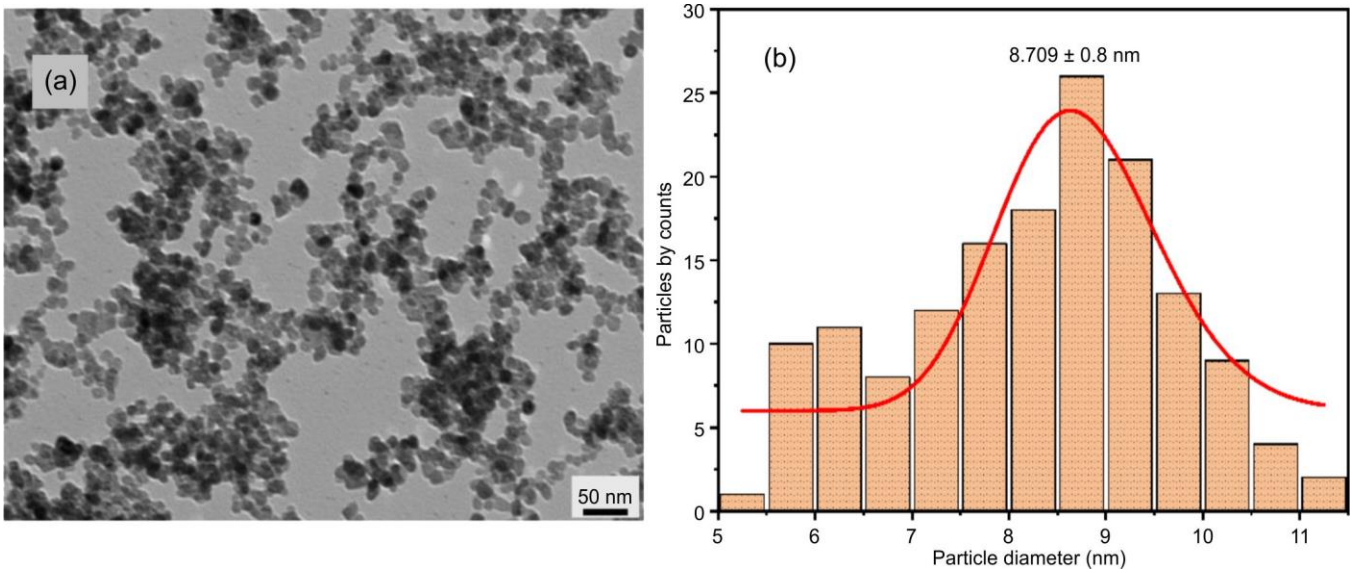

Fig. 2. (a) TEM micrograph of $Zn_{0.97}O:Bi^{3+}_{0.03}$ and (b) histogram distribution of the particle size

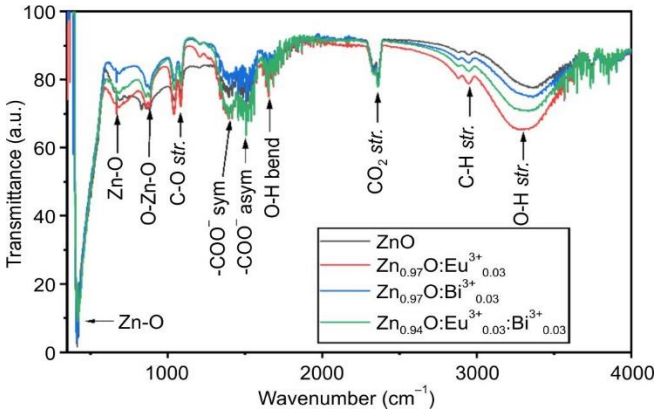

Fig. 3. FTIR spectra of as-prepared pure ZnO, $Zn_{0.97}O:Eu^{3+}_{0.03}$, $Zn_{0.97}O:Bi^{3+}_{0.03}$ and Bi^{3+} (3 at.%) co-doped $Zn_{0.94}O:Eu^{3+}_{0.03}$ NPs

vibration mode of the C-O bond. The symmetric and asymmetric stretching vibration modes of -COO^- are observed at 1395 cm^{-1} and 1515 cm^{-1}, which might be from the zinc acetate precursor [11]. The peak at 2946 cm^{-1} can be assigned to the C-H group stretching vibration of ethylene glycol molecules. The absorption peak appeared at 2358 cm^{-1} may be due to the presence of CO_2, likely resulting from the atmospheric adsorption on the surface of the sample [29]. All samples exhibited a broad absorption band between 3600-3000 cm^{-1}, which corresponds to O-H stretching vibrations, while the peak at 1650 cm^{-1} is attributed to the O-H bending vibrations of EG/water molecules [30]. The FTIR spectrum confirmed the presence of EG molecules adsorbed on the NPs surface, suggesting its role as a capping agent.

Elemental composition: Fig. 4a-b displays the EDAX spectrum of pure ZnO and $Zn_{0.96}O:Eu^{3+}_{0.03}:Bi^{3+}_{0.01}$. Spectral analysis confirms the presence of Zn and O in a 1:1 atomic ratio in pristine ZnO, while Zn, O, C, Eu and Bi are detected in the co-doped ZnO NPs. The elemental composition (atomic %) of the samples is summarized in the inset table of Fig. 4a-b. The increase in Eu content and corresponding decrease in Bi content suggest the successful incorporation of the dopant ions into the ZnO lattice [31].

Optical studies: Fig. 5a shows the UV-Visible absorption spectra of pure, doped and co-doped samples. The absorption peak was observed at λ_{max}: 351 nm for pure ZnO, while $Zn_{0.97}O:Bi^{3+}_{0.03}$, $Zn_{0.97}O:Eu^{3+}_{0.03}$, $Zn_{0.96}O:Eu^{3+}_{0.03}:Bi^{3+}_{0.01}$ and $Zn_{0.94}O:Eu^{3+}_{0.03}:Bi^{3+}_{0.03}$ show absorption at 353 nm, 349 nm,

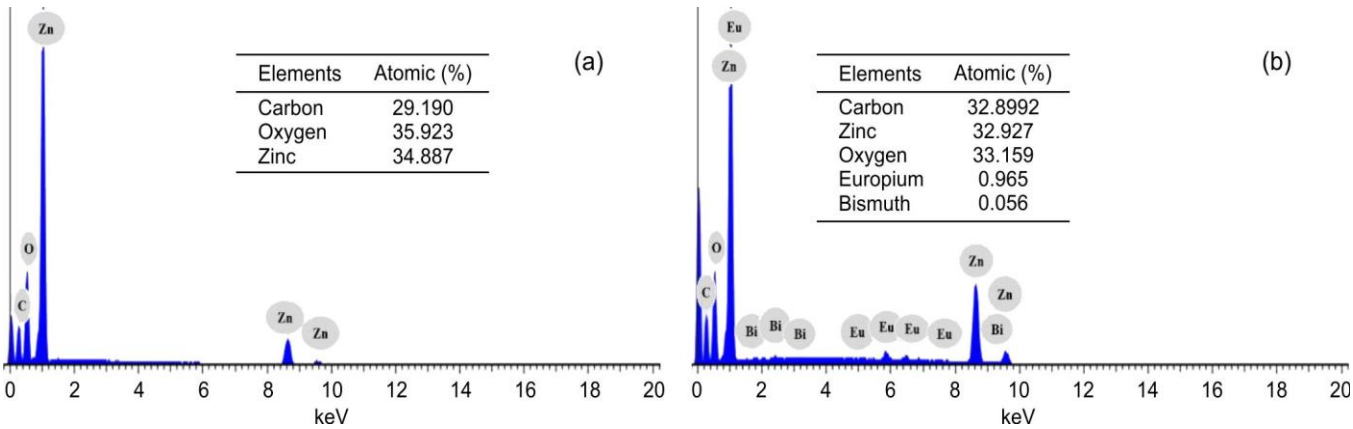

Fig. 4 EDAX spectra of (a) ZnO and (b) Bi^{3+} (1 at.%) co-doped $Zn_{0.96}O:Eu^{3+}_{0.03}$ NPs

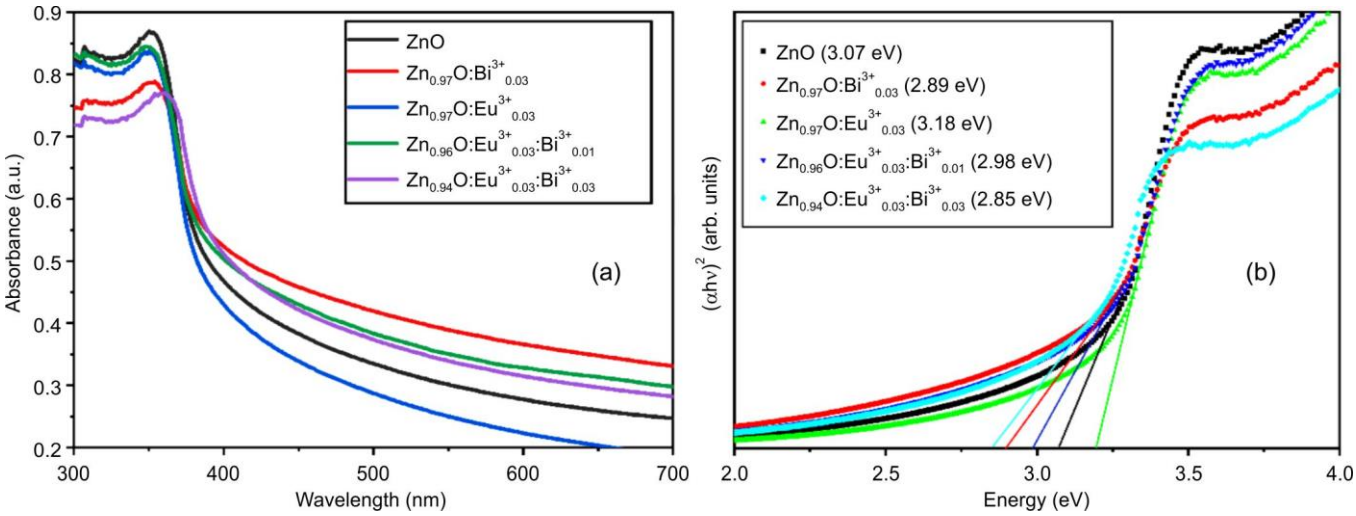

Fig. 5. (a) UV-Visible absorption spectra and (b) band gap energies of pure, doped and co-doped ZnO NPs

349 nm and 360 nm, respectively. The optical absorbance spectra of $Zn_{0.97}O:Bi^{3+}_{0.03}$ and $Zn_{0.94}O:Eu^{3+}_{0.03}:Bi^{3+}_{0.03}$ are slightly shifted to higher wavelength (351-360 nm) due to the generation of lattice defects in ZnO [32] on doping, while the absorption bands influence the electronic structure and carrier dynamics [33]. The band-gap were evaluated by using Tauc's plot:

$$(\alpha h\nu)^n = A(h\nu - E_g) \quad (2)$$

where hν represents the photon energy, α is the absorption coefficient, A is a constant, E_g denotes the optical band-gap and n is a factor that depends on the electronic transition [10]. As ZnO possesses a direct band gap, the exponent n = ½ was used to determine its optical band gap. Fig. 5b shows that the E_g value increases in $Zn_{0.97}O:Eu^{3+}_{0.03}$ (3.18 eV) and then decreases in $Zn_{0.96}O:Eu^{3+}_{0.03}:Bi^{3+}_{0.01}$ (2.98 eV), $Zn_{0.97}O:Bi^{3+}_{0.03}$ (2.89 eV) and $Zn_{0.94}O:Eu^{3+}_{0.03}:Bi^{3+}_{0.03}$ (2.85 eV) compared to pure ZnO (3.07 eV). The band gap narrowing can be attributed to several factors, including defect generation, lattice distortion and the incorporation of small amounts of Eu^{3+} and Bi^{3+} impurities into the ZnO lattice [34-36].

Photoluminescence (PL) analysis: The excitation spectra of $Zn_{0.97}O:Eu^{3+}_{0.03}$ and Bi^{3+} (1, 3 at.%) co-doped $Zn_xO:Eu^{3+}_{0.03}$ samples, were observed at λ_{em} = 615 nm and are presented in Fig. 6a. Three distinct peaks appear at 394, 415 and 464 nm corresponding to the $^7F_0 \rightarrow {}^5L_6$, $^7F_0 \rightarrow {}^5D_3$ and $^7F_0 \rightarrow {}^5D_2$ transitions, arising from internal 4*f*-4*f* electronic transitions within the Eu^{3+} ion [37-39]. In all the spectra, an increase in the *f-f* absorption intensities is observed with the sensitisation by Bi^{3+} ion. The strongest excitation peak at 394 nm corresponding to the $^7F_0 \rightarrow {}^5L_6$ transition, reaches its maximum intensity when the Bi^{3+} concentration is 1 at.% than that of $Zn_{0.97}O:Eu^{3+}_{0.03}$ and $Zn_{0.94}O:Eu^{3+}_{0.03}:Bi^{3+}_{0.03}$. From the excitation spectrum monitored at 615 nm, the peak at 464 nm exhibits maximum enhancement in Bi^{3+} (3 at.%) co-doped $Zn_{0.94}O:Eu^{3+}_{0.03}$ sample compared to $Zn_{0.96}O:Eu^{3+}_{0.03}:Bi^{3+}_{0.01}$ and $Zn_{0.97}O:Eu^{3+}_{0.03}$. The observed enhancement is attributed to crystal field distortion around Eu^{3+} ions, arising from the different charge

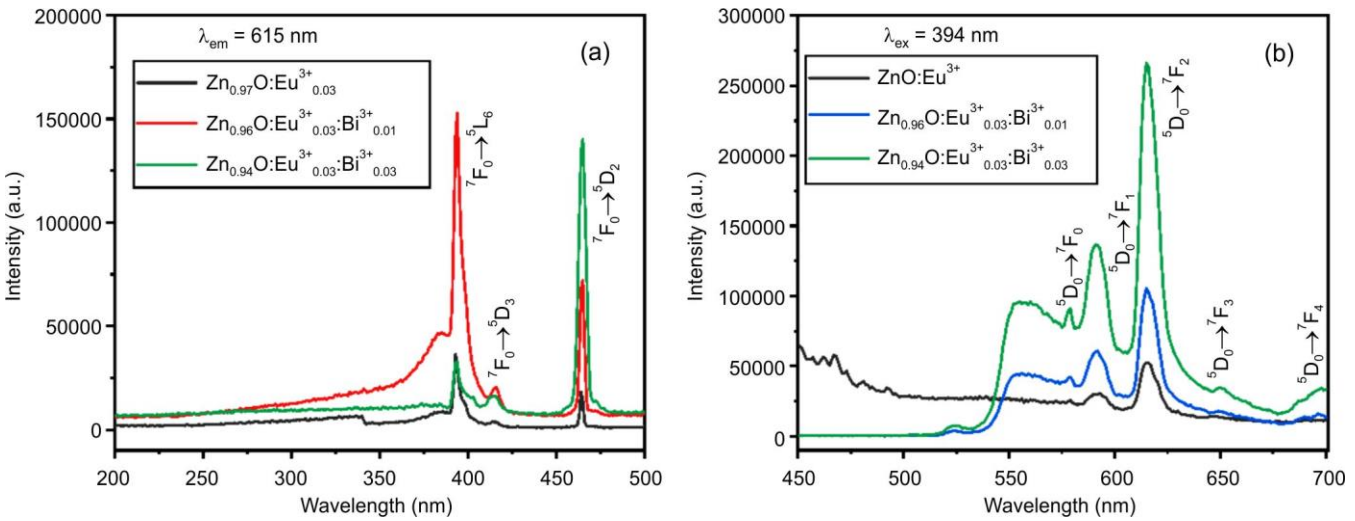

Fig. 6. (a) Excitation spectra of $Zn_{0.97}O:Eu^{3+}_{0.03}$, Bi^{3+} (1, 3 at.%) co-doped $Zn_xO:Eu^{3+}_{0.03}$ samples monitored at 615 nm emission wavelength and (b) emission spectra of $Zn_{0.97}O:Eu^{3+}_{0.03}$, Bi^{3+} (1, 3 at.%) co-doped $Zn_xO:Eu^{3+}_{0.03}$ NPs at 394 nm excitation wavelength

states of Zn^{2+}, Bi^{3+} and Eu^{3+} [12,40]. In the absence of adequate charge compensation, the substitution of Zn^{2+} with higher valent ions such as Eu^{3+} and Bi^{3+} induces a charge imbalance, which is accommodated by the formation of Zn-site vacancies in order to maintain overall lattice neutrality [41].

The observed emission spectra of doped and co-doped samples under the λ_{ex} = 394 nm are shown in Fig. 6b. The strongest emission peak at 615 nm, originating from the hypersensitive electric dipole $^5D_0 \rightarrow {}^7F_2$ transition of Eu^{3+} ions, is observed in all samples due to the low-symmetry environment surrounding the Eu^{3+} sites and the peak at 590 nm ($^5D_0 \rightarrow {}^7F_1$), which is related to magnetic dipole become more intense if Eu^{3+} ions are positioned at sites with inversion symmetry [42]. The emission intensity of Eu^{3+} ion is enhanced with increasing Bi^{3+} ion concentration, indicating that Bi^{3+} ion absorbs energy from the host and transfers it to the Eu^{3+} ion [43]. A broad hump ranging from 530-570 nm might be due to point defects of oxygen vacancies (V_0) or energy transfer between the dopants *i.e.* $Bi^{3+} \rightarrow Eu^{3+}$. The emission corresponding to the forbidden $^5D_0 \rightarrow {}^7F_0$ transition at 578 nm is due to Eu^{3+} ions occupying a site with symmetries such as C_n, C_s and C_{nv} [13].

PL decay lifetime study: The PL decay curves of the emissive $^5D_0$ excited state of Eu^{3+} (3 at.%) in Bi^{3+} (0, 1 and 3 at.%) co-doped ZnO NPs were studied. The luminescence decay curve of the prepared NPs recorded under λ = 394 nm excitation and monitored at λ = 615 nm emission are shown in Fig. 7. All the decay curves are well fitted with a bi-exponential function [44]:

$$I(t) = I_0 + I_1 \exp\left(\frac{-t}{\tau_1}\right) + I_2 \exp\left(\frac{-t}{\tau_2}\right) \quad (3)$$

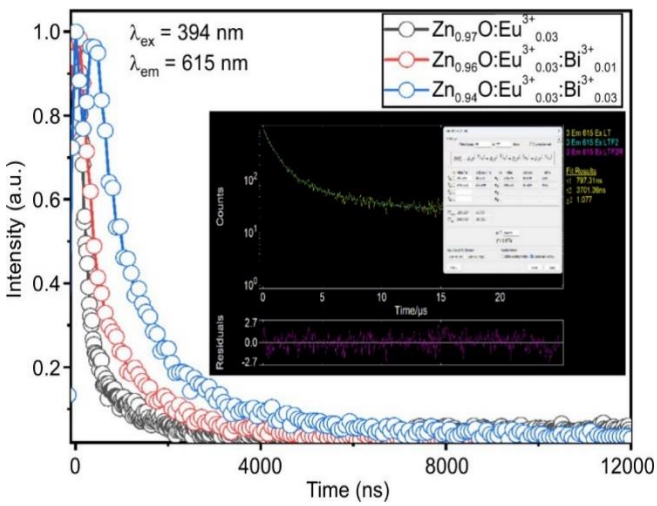

Fig. 7. PL decay curves corresponding to the $^5D_0$ level of Eu^{3+} in Zn_xO:$Eu^{3+}_{0.03}$:Bi^{3+} (0, 1 and 3 at.%) NPs with inset of the measured $Zn_{0.94}O$:$Eu^{3+}_{0.03}$:$Bi^{3+}_{0.03}$ decay signal

where I (t) and I_0 indicates the luminescence intensities at any time t and at t = 0, respectively, I_1 and I_2 are the intensities at different time intervals, τ_1 and τ_2 are the corresponding decay lifetimes.

The average lifetime (τ_{av}) of the Zn_xO:$Eu^{3+}_{0.03}$:Bi^{3+} (0, 1 and 3 at.%) samples were calculated using eqn. 4:

$$\tau_{av} = \frac{I_1\tau_1^2 + I_2\tau_2^2}{I_1\tau_1 + I_2\tau_2} \quad (4)$$

The enhancement in the τ_{av} of Eu^{3+} (0.61 μs) after Bi^{3+} (1, 3 at.%) incorporation (1.253, 2.049) may be attributed to the suppression of non-radiative recombination pathways or partial recovery of matrix defects [45]. Bi-exponential life time (τ_{av}) of Zn_xO:$Eu^{3+}_{0.03}$:Bi^{3+} (0, 1 and 3 at.%) NPs at λ_{ex} = 394 nm and λ_{em} = 615 nm is shown in Table-2.

Commission Internationale de IEclairage (CIE) chromaticity study: CIE chromaticity diagram of ZnO at 328 nm, $Zn_{0.97}O$:$Bi^{3+}_{0.03}$ at 399 nm, $Zn_{0.97}O$:$Eu^{3+}_{0.03}$ and Bi^{3+} (1, 3 at.%) co-doped Zn_xO:$Eu^{3+}_{0.03}$ at 394 nm excitation wavelength is shown in Fig. 7 and their colour co-ordinates are summarised in the inset of Fig. 8. The CIE chromaticity diagram indicates the potential for colour tuning from dark blue to light red through white emission. The emission colour of ZnO and $Zn_{0.97}O$:$Bi^{3+}_{0.03}$ samples appear in the dark blue region, while $Zn_{0.97}O$:$Eu^{3+}_{0.03}$ sample exhibits emission in the white region. Interestingly, Bi^{3+} (1, 3 at.%) co-doped Zn_xO:$Eu^{3+}_{0.03}$ samples exhibit emission in the light red region, which also serves as evidence that energy transfer from Bi^{3+} to Eu^{3+} occurs.

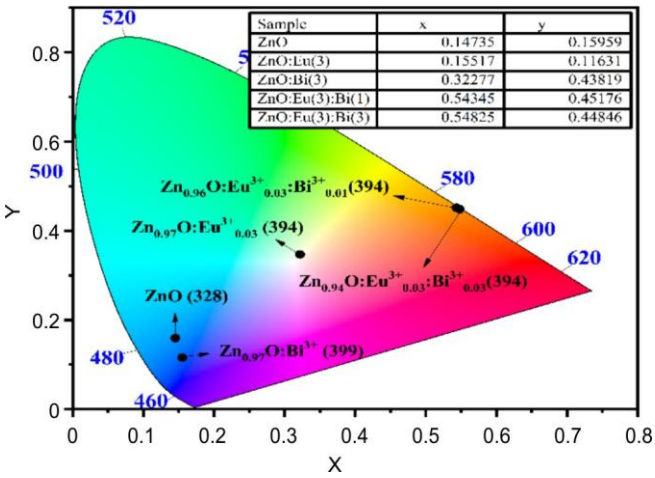

Fig. 8. CIE Chromaticity diagram of pure, doped and co-doped ZnO nanophosphor

Photocatalytic performance: The schematic representation of photodegradation of CV dye by using nanocatalyst is shown in Fig. 9, whereas the photocatalytic activity of ZnO, $Zn_{0.97}O$:$Bi^{3+}_{0.03}$, $Zn_{0.97}O$:$Eu^{3+}_{0.03}$, $Zn_{0.96}O$:$Eu^{3+}_{0.03}$:$Bi^{3+}_{0.01}$ and

TABLE-2
Bi-EXPONENTIAL LIFE TIME (τ_{av}) OF Zn_xO:$Eu^{3+}_{0.03}$:Bi^{3+} (0, 1 AND 3 at.%) NPs AT λ_{ex} = 394 nm AND λ_{em} = 615 nm

Bi (at.%)	I_1	τ_1	I_1	τ_2	τ_{av} (μs)	Chi^2
0	898.5455	168.7564	216.2214	939.6071	0.610	1.2593
1	918.4305	351.3353	254.6879	1865.7108	1.253	1.0267
3	878.6745	797.3146	143.5509	3701.3562	2.049	1.0774

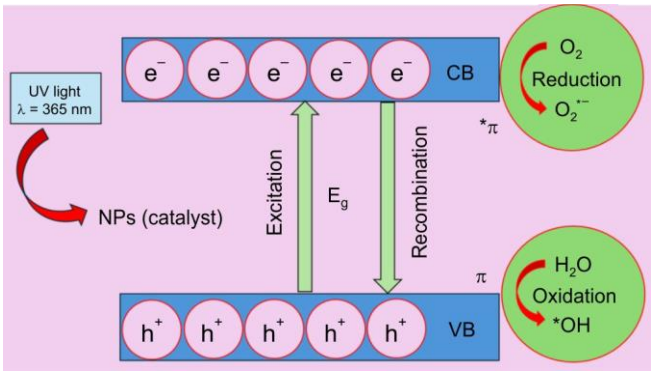

Fig. 9. Photodegradation mechanism of CV dye by using nanocatalyst

$Zn_{0.94}O:Eu^{3+}_{0.03}:Bi^{3+}_{0.03}$ NPs under UV irradiation (λ = 365 nm) are presented in Figs. 10a-e and 11a. CV shows an absorption peak at 590 nm and a decrease in this peak indicates the degradation of the dye.

The photodegradation efficiency of the various photocatalysts over 180 min was calculated using eqn. 5 [46]:

$$\text{Photodegradation efficiency (\%)} = \frac{A_o - A_t}{A_o} \times 100 \quad (5)$$

where A_o is the initial absorbance value of dye solution, and A_t represents its concentration value after photodegradation at time t. Table-3 presents the degradation efficiency of all synthesised nanocrystals against crystal violet (CV). Although

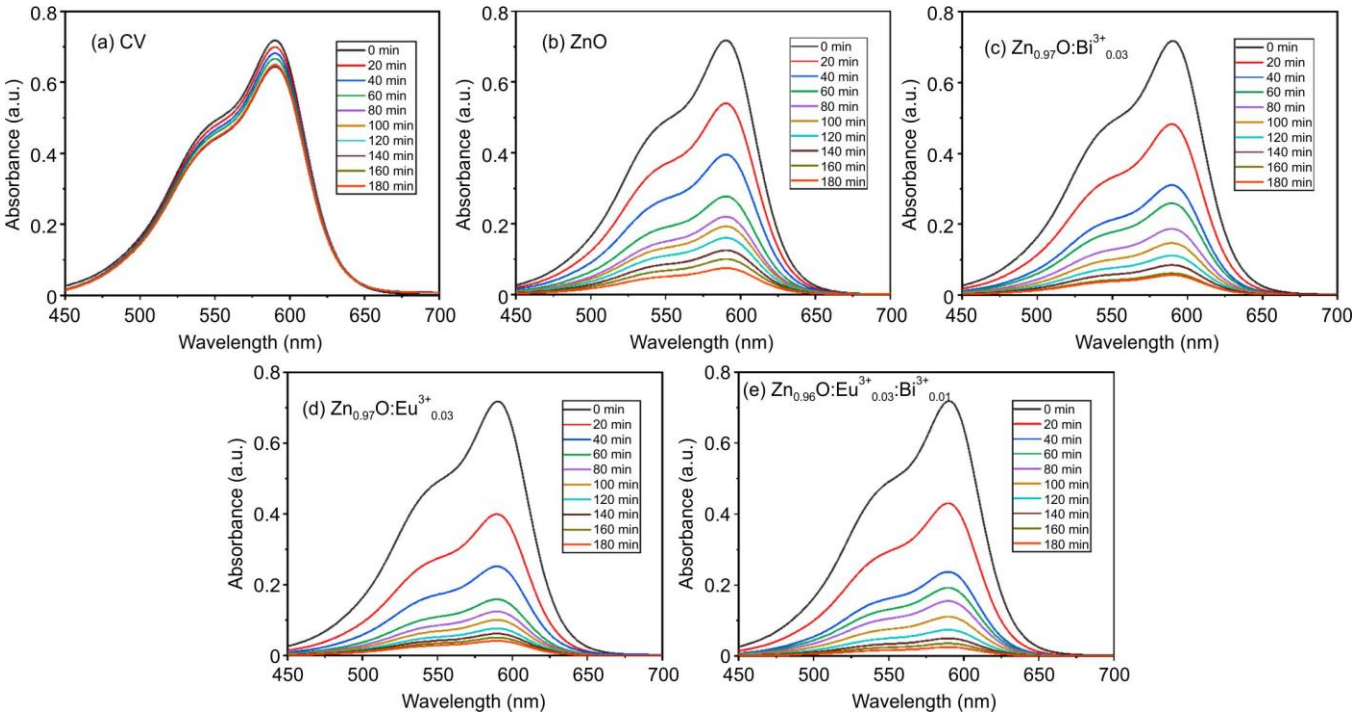

Fig. 10. Photocatalytic degradation of CV by pure ZnO, $Zn_{0.97}O:Bi^{3+}_{0.03}$, $Zn_{0.97}O:Eu^{3+}_{0.03}$, and $Zn_{0.96}O:Eu^{3+}_{0.03}:Bi^{3+}_{0.01}$ NPs under UV irradiation over 180 min

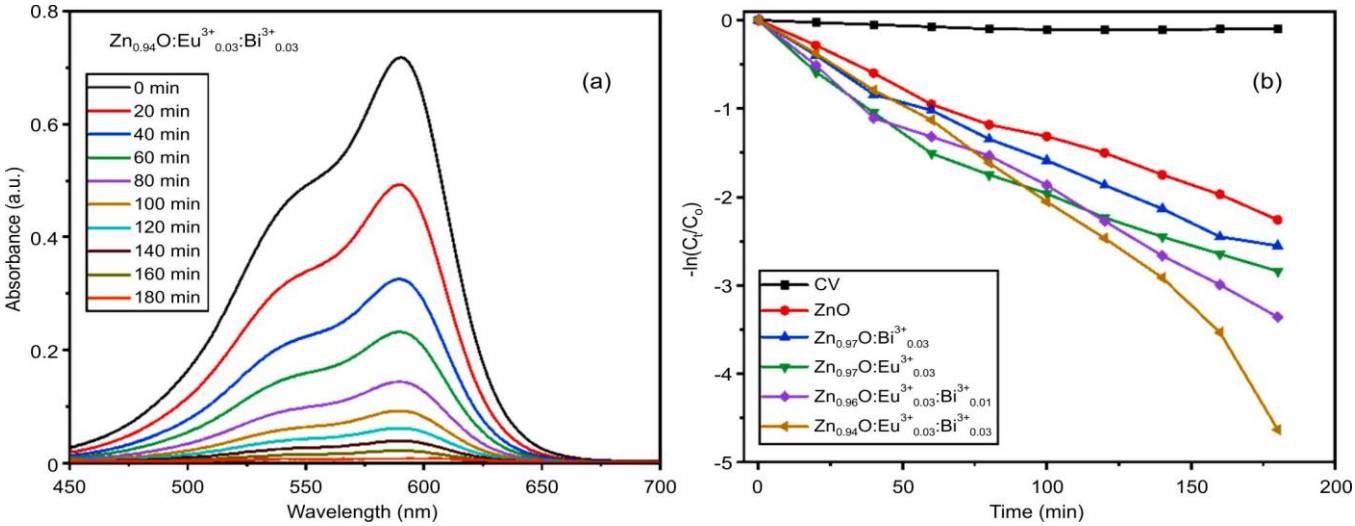

Fig. 11. (a) UV-Vis absorption spectra of $Zn_{0.94}O:Eu^{3+}_{0.03}:Bi^{3+}_{0.03}$ recorded during the photodegradation of CV and (b) Photodegradation efficiency of CV aqueous solutions using pure, doped and co-doped NPs under UV irradiation over 180 min

TABLE-3
PHOTODEGRADATION EFFICIENCY (%), KINETIC RATE CONSTANT (k) AND R^2 VALUES OF GROWN NANOCRYSTALS

Sample	Degradation efficiency (%)	Rate constant, k (min^{-1})	R^2
CV	9.6	0.00055	0.75213
ZnO	89.5	0.01201	0.98941
$Zn_{0.97}O:Bi^{3+}_{0.03}$	92.2	0.01411	0.98997
$Zn_{0.97}O:Eu^{3+}_{0.03}$	94.1	0.01495	0.95891
$Zn_{0.96}O:Eu^{3+}_{0.03}:Bi^{3+}_{0.01}$	96.5	0.01774	0.99060
$Zn_{0.94}O:Eu^{3+}_{0.03}:Bi^{3+}_{0.03}$	99.0	0.02388	0.98981

several studies have reported photocatalytic degradation of CV using high-temperature synthesised and calcined materials.

As CV dye attributed to the triphenylmethane group having cationic nature, which prefers in alkaline solution, hence the degradation of CV significantly depends on pH value [47]. The co-doped photocatalyst significantly enhanced degradation efficiency toward CV dye compared to undoped and singly doped ZnO samples. The degradation efficiency was found to be highest when using $Bi^{3+}_{0.03}$ co-doped $Zn_{0.94}O:Eu^{3+}_{0.03}$ NPs as the photocatalyst (99%) compared to pure ZnO NPs (89.5%). The plot of -ln (C_t/C_o) *vs*. time given in Fig. 11b decreases linearly with negative slope, signifying that the degradation route follows pseudo-first-order kinetics, with the highest rate constant of 0.02388 min^{-1} for $Zn_{0.94}O:Eu^{3+}_{0.03}:Bi^{3+}_{0.03}$ (Fig. 12a-f). The enhancement in the photocatalytic activity of $Bi^{3+}_{0.03}$ co-doped $Zn_{0.94}O:Eu^{3+}_{0.03}$ can be attributed to the synergistic effect of Bi^{3+} and Eu^{3+} dopants, which enhances visible light absorption and promotes effective charge carrier separation. Bi^{3+} acting as electron trapping centres whereas Eu^{3+} playing a role in bandgap modulation and energy transfer process through its 4*f*-orbital transitions. Due to most narrowing band gap, $Zn_{0.94}O:Eu^{3+}_{0.03}:Bi^{3+}_{0.03}$ mostly absorbed visible light and enhanced its photocatalytic activity than other pure, doped and co-doped catalyst.

Comparative studies: As summarized in Table-4, the synthesized ZnO/Eu^{3+}/Bi^{3+} photocatalyst achieved 99% degradation of crystal violet (CV) dye within 180 min at an initial concentration of 12.5 ppm, outperforming most previously reported pure and doped ZnO photocatalysts. Compared with conventional ZnO-based systems, the enhanced performance can be attributed to the synergistic effect of Eu^{3+} and Bi^{3+} co-doping, which improves charge separation and suppresses the electron–hole recombination, resulting in superior photocatalytic efficiency under UV irradiation.

Mechanism: During oxidation, the photogenerated holes reacts with water molecules or hydroxide ions to generate hydroxyl radicals ($^{\bullet}OH$) and in reduction; electrons are trapped by the dopants and convert O_2 to superoxide radicals ($^{\bullet}O_2^-$). These reactive oxygen species strongly oxidize and degrade organic pollutants. The degradation mechanism is given below:

$$ZnO + h\nu \rightarrow ZnO\ (e^- + h^+) \quad (6)$$

$$Bi^{3+} + e^- \rightarrow Bi^{3+}(e^- \text{ trapped/defect state}) \quad (7)$$

$$Eu^{3+} + e^- \rightarrow Eu^{3+}(\text{recombination centre}) \quad (8)$$

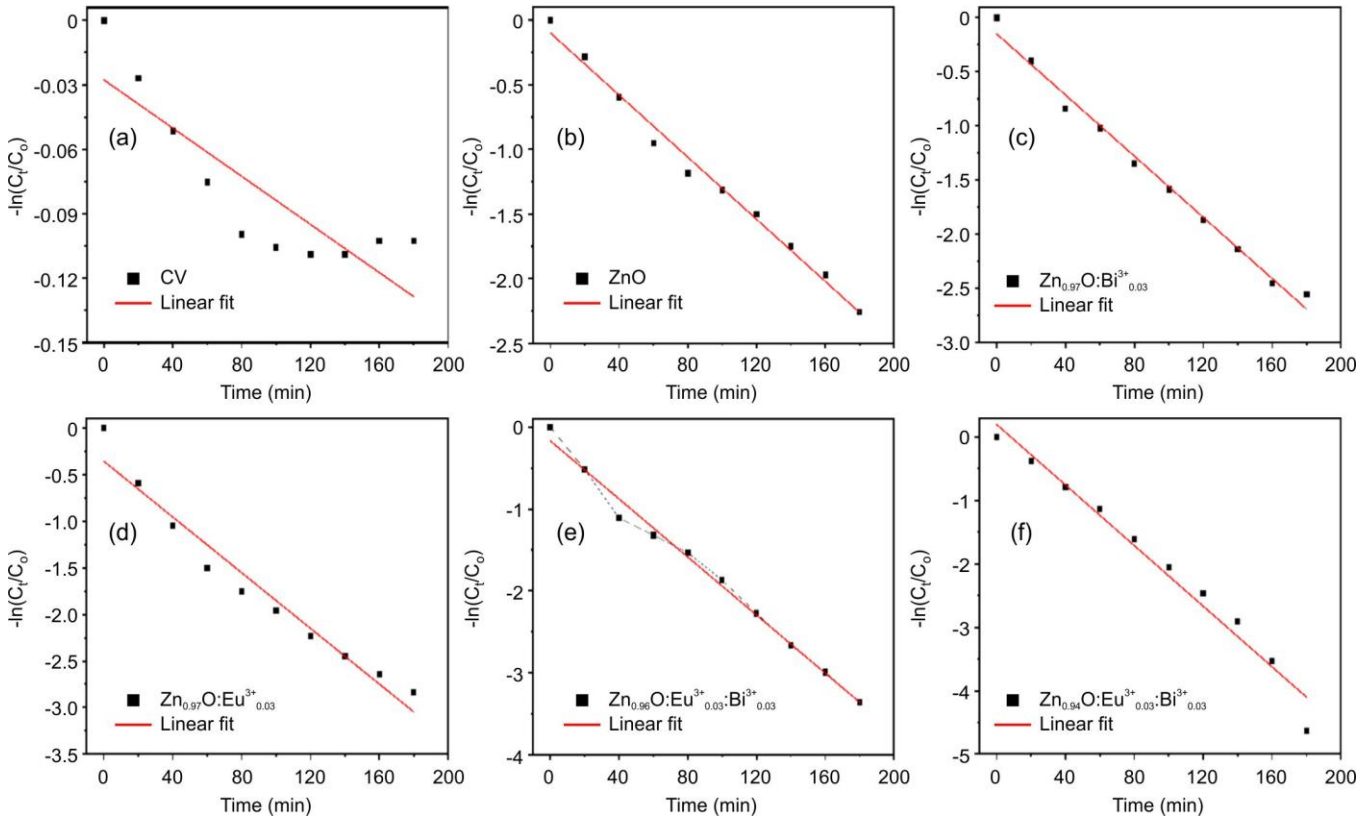

Fig. 12. Kinetic plots for photocatalytic degradation of CV under UV irradiation (a) CV blank solution and (b-f) pure, doped, and co-doped ZnO NPs

TABLE-4
SUMMARY OF REPORTED CV DEGRADATION STUDIES USING PURE AND DOPED-ZnO PHOTOCATALYSTS UNDER UV EXPOSURE

Catalyst	Synthesis method	Time (min)	Initial dye concentration (ppm)	Degradation efficiency (%)	Ref.
ZnO	Refluxing	80	10.0	88.9%	[48]
ZnO/Ag	Refluxing	80	10.0	95.0	[48]
ZnO/C	Biosynthesis	300	10.0	92.7	[49]
ZnO	Spray pyrolysis	210	12.5	86.0	[50]
ZnO/Co	Spray pyrolysis	210	12.5	91.3	[50]
ZnO/In	Spray pyrolysis	210	12.5	85.0	[50]
ZnO	Co-precipitation	240	5.0	82.0	[51]
ZnO/GO	Solid state reaction	240	5.0	99.0	[51]
ZnO	Facile hydrothermal	120	30.0	70.2	[52]
ZnO/Fe_3O_4	Facile hydrothermal	120	30.0	90.9	[52]
ZnO/Eu^{3+}/Bi^{3+}	Co-precipitation	180	12.5	99.0	This work

$$e^- + O_2 \rightarrow {}^\bullet O_2^- \text{ (superoxide)} \quad (9)$$

$$h^+ + OH^- \rightarrow {}^\bullet OH \quad (10)$$

$$\text{Organic pollutants} + {}^\bullet O_2^- + {}^\bullet OH \rightarrow CO_2 + H_2O + \text{Degraded product}$$

Detection of hydroxyl radicals (•OH): The formation of reactive oxygen species (ROS) exerts a significant influence in the photocatalytic degradation of various dyes through reduction and oxidation reactions. Among the various ROS, owing to their effective oxidizing efficiency, detection and monitoring of these hydroxyl radicals (•OH) and superoxide radical anions ($^\bullet O_2^-$) known as the most active species are vital for insight into the reaction mechanism and estimating photocatalytic efficiency. Since hydroxyl •OH are identified as the main ROS involved in degradation, fluorescence-based probe terephthalic acid (TA) for the detection of •OH *via* the formation of fluorescence 2-hydroxyterephthalic acid (2-HTA) over $Zn_{0.94}O:Eu^{3+}_{0.03}:Bi^{3+}_{0.03}$ NPs was selected owing to its superior photocatalytic performance [2]. Upon UV irradiation, photogenerated holes and electrons are generated on the photocatalyst surface. The photogenerated holes react with surface hydroxyl groups or water molecules to create hydroxyl radicals. The principle of the method can be described as: (i) the •OH formed photocatalytically on the surface of $Zn_{0.94}O:Eu^{3+}_{0.03}:Bi^{3+}_{0.03}$ NPs react with TA to produce 2-HTA (ii) the resulting 2-HTA shows a prominent fluorescence emission peak at 425 nm when λ_{ex} = 315 nm. The intensity of the generated fluorescence of 2-HTA gradually increases with UV irradiation time (0-180 min), as shown in Fig. 13a and allows correlation with photocatalytic activity.

Reduction of superoxide radical anions ($^\bullet O_2^-$): The generation of superoxide radicals ($^\bullet O_2^-$) while the photocatalysis was studied using the reduction of nitro blue tetrazolium (NBT) as shown in Fig. 13b. In this study, NBT act as a preferential probe molecule for $^\bullet O_2^-$ species, where pale yellow colour NBT underwent reduction into purple-blue coloured insoluble formazan (NBT+F). The NPs-NBT mixture show noticeable NBT+F within 20 min of UV exposure, indicating efficient electron transfer occur from the conduction band of the photocatalyst.

The simultaneous observation of both •OH and $^\bullet O_2^-$ radicals strongly reveals that these are primary ROS species resulting in the photocatalytic activity. Among them, •OH radicals are likely developed through valence-band hole-driven oxidation pathway, while $^\bullet O_2^-$ radicals are subsequently arising *via*

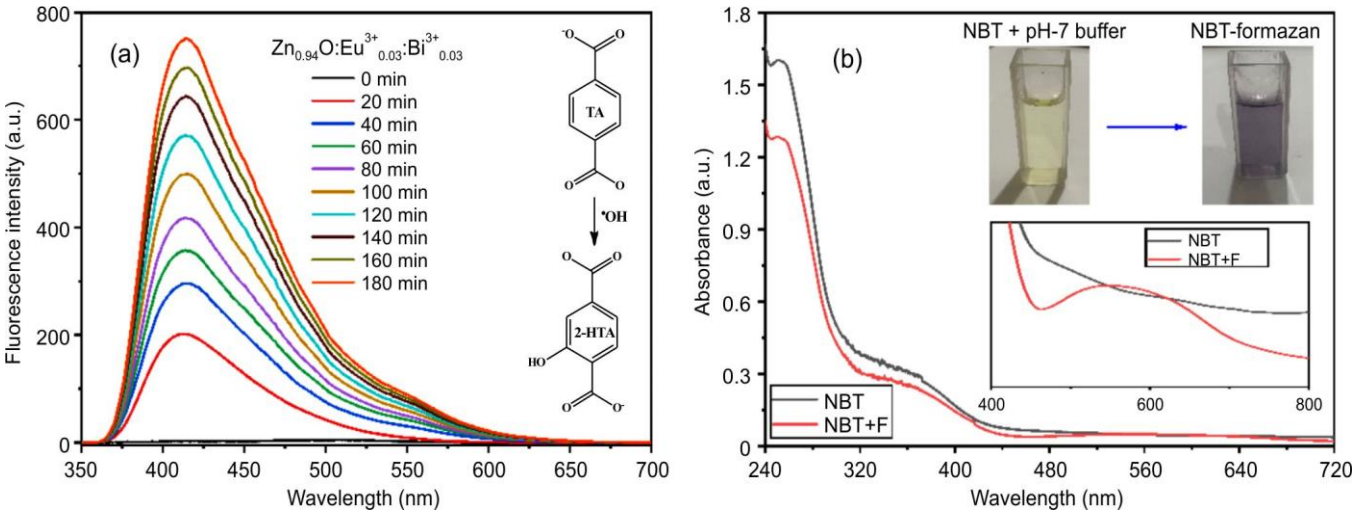

Fig. 13. Schematic illustration of ROS generation (a) hydroxyl (•OH) and (b) superoxide ($^\bullet O_2^-$) radicals under UV irradiation

electron transfer to adsorbed molecular oxygen. Hence, the mechanism of photocatalytic degradation follows *via* a synergistic ROS route including both oxidation and reduction phenomena, which altogether play a role to the efficiency degradation of organic pollutants.

Recyclability studies: The recyclability of the photocatalyst was carried out up to five successive cycles for the degradation of CV to assess its practical applicability. The degradation efficiency slightly decreases from ~98.7% (cycle-1) to ~96.1% (cycle-5) was observed after repeated use (Fig. 14). The gradual decrease in catalytic activity may be due to partial loss of NPs during washing or aggregation of NPs during recycling. To further verify the structural stability of the NPs, the PXRD was carried out on used sample. The XRD patterns in Fig. 15, showed no extra peak or visible shift in peak positions, confirming that the pure structure of ZnO remain unchanged after five cycles. The slight variation in crystallite size after reuse does not significantly influence phase purity, confirming the structural durability of the catalyst.

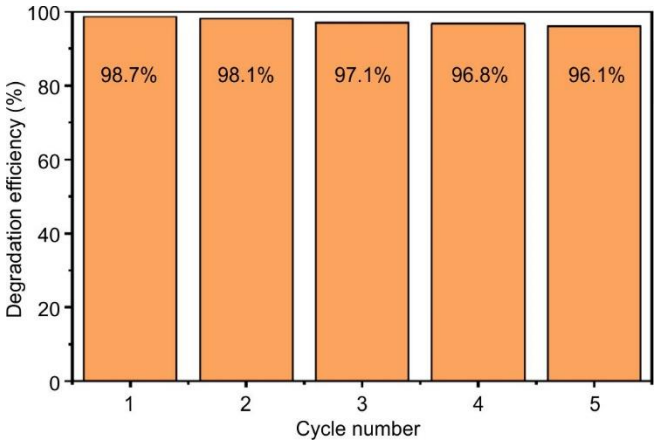

Fig. 14. Photocatalytic degradation efficiency of $Zn_{0.94}O:Eu^{3+}_{0.03}:Bi^{3+}_{0.03}$ catalyst over five successive cycles

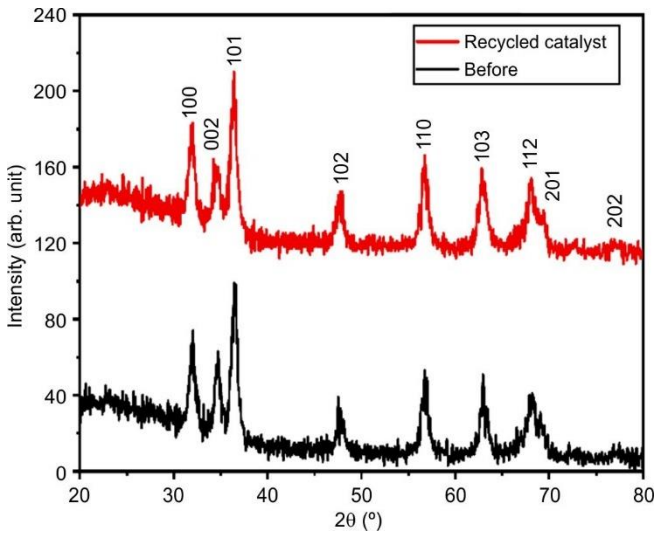

Fig. 15. PXRD patterns of as-prepared and reused $Zn_{0.94}O: Eu^{3+}_{0.03}:Bi^{3+}_{0.03}$ catalyst

Furthermore, the UV-Vis spectra (Fig. 16a-e) recorded over five consecutive cycles reveal a consistent decrease in the characteristic CV absorption peak (~590 nm) with irradiation time, confirming effective dye degradation by the $Zn_{0.94}O$:

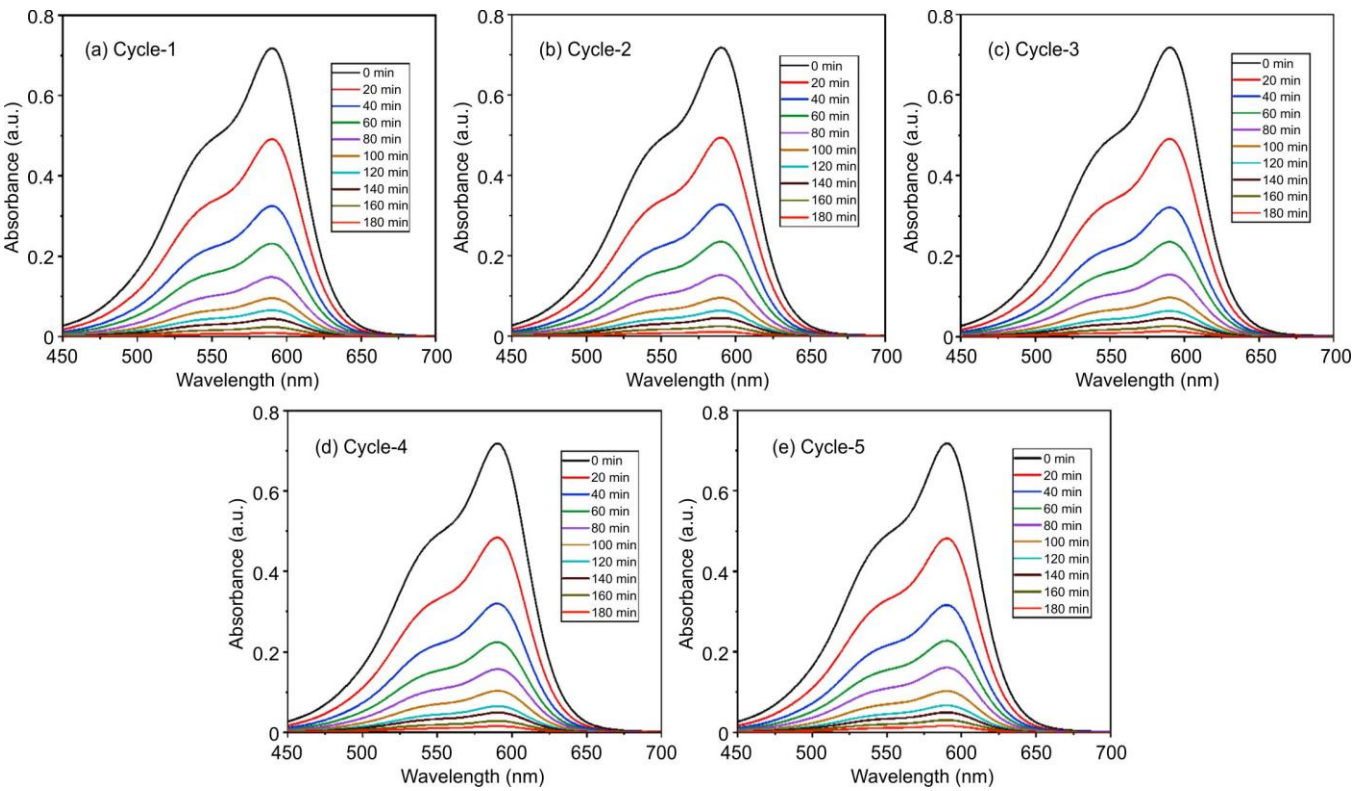

Fig. 16. UV-visible spectra of photocatalytic degradation efficiency of $Zn_{0.94}O:Eu^{3+}_{0.03}:Bi^{3+}_{0.03}$ catalyst over five successive cycles

$Eu^{3+}_{0.03}$:$Bi^{3+}_{0.03}$ photocatalyst. Similar spectral trends across all cycles indicate that the catalyst largely retains its photocatalytic activity during reuse. Despite a slight decline in degradation efficiency from 98.7% to 96.1%, near-complete removal of CV was achieved after 180 min in each cycle. Combined with the unchanged PXRD pattern after recycling, these results demonstrate the excellent stability, durability, and reusability of the catalyst for wastewater treatment applications.

Conclusion

Pure ZnO, $Zn_{0.97}O$:$Eu^{3+}_{0.03}$, $Zn_{0.97}O$:$Bi^{3+}_{0.03}$, $Zn_{0.96}O$:$Eu^{3+}_{0.03}$:$Bi^{3+}_{0.01}$ and $Zn_{0.94}O$:$Eu^{3+}_{0.03}$:$Bi^{3+}_{0.03}$ NPs have been synthesised by co-precipitation technique. The PXRD study confirmed that all nanoparticles correspond to hexagonal wurtzite structure with no other secondary phases. The NPs are at the nanoscale, with an average diameter ranging from 8 to 11 nm. The emission intensity of Eu^{3+} at 615 nm, corresponding to the $^5D_0 \rightarrow {}^7F_2$ transition, was significantly enhanced by Bi^{3+} co-doping. Bi^{3+} (1 at.%) co-doped $Zn_{0.96}O$:$Eu^{3+}_{0.03}$ increased the intensity under 393 nm excitation, while Bi^{3+} (3 at.%) co-doped $Zn_{0.94}O$:$Eu^{3+}_{0.03}$ enhanced the excitation as compared to singly $Eu^{3+}_{0.03}$ doped $Zn_{0.97}O$. Furthermore, Bi^{3+} (3 at.%) co-doped $Zn_{0.94}O$:$Eu^{3+}_{0.03}$ demonstrated superior photocatalytic efficiency compared to the pure and singly doped ZnO samples, making it a potential candidate for light-driven wastewater treatment applications.

ACKNOWLEDGEMENTS

The authors gratefully acknowledge Department of Physics, Lumami Nagaland University for PL measurements. The authors also thank Manipur University for providing access to the PL lifetime decay facility procured under DST-FIST Grant (SR/FST/CS-1/2023/328), XRD, FTIR, measurements and the Central Research Facility (CRF), IIT Delhi, for EDAX, TEM analysis.

CONFLICT OF INTEREST

The authors declare that there is no conflict of interests regarding the publication of this article.

DECLARATION OF AI-ASSISTED TECHNOLOGIES

During the preparation of this manuscript, the authors used an AI-assisted tool(s) to improve the language. The authors reviewed and edited the content and take full responsibility for the published work.

REFERENCES

1. S. Irtiqa and A. Rahman, *J. Inst. Eng. India Ser. E*, **103**, 259 (2022); https://doi.org/10.1007/s40034-021-00233-1
2. V. Nedelkovski, M. Radovanovic and M. Antonijevic, *Chem. Eng.*, **9**, 120 (2025); https://doi.org/10.3390/chemengineering9060120
3. M. Bououdina, S. Azzaza, R. Ghomri, M.N. Shaikh, J.H. Dai, Y. Song, W. Song, W. Cai and M. Ghers, *RSC Adv.*, **7**, 32931 (2017); https://doi.org/10.1039/C7RA01015J
4. D. Daksh and Y.K. Agrawal, *J. Nanosci. Nanotechnol.*, **5**, 1 (2016); https://doi.org/10.1166/rnn.2016.1071
5. E. Hannachi, Y. Slimani, M. Nawaz, Z. Trabelsi, G. Yasin, M. Bilal, M.A. Almessiere, A. Baykal, A. Thakur and P. Thakur, *J. Phys. Chem. Solids*, **170**, 110910 (2022); https://doi.org/10.1016/j.jpcs.2022.110910
6. S. Qiu, J. Wu, L. Chen and Y. Li, *RSC Sustain.*, **3**, 995 (2025); https://doi.org/10.1039/D4SU00691G
7. M. Carofiglio, S. Barui, V. Cauda and M. Laurenti, *Appl. Sci.*, **10**, 5194 (2020); https://doi.org/10.3390/app10155194
8. A.U. Hasanah, M.S. Ikbal and D. Tahir, *ChemBioEng Rev.*, **11**, 595 (2024); https://doi.org/10.1002/cben.202300058
9. V.L. Chandraboss, L. Natanapatham, B. Karthikeyan, J. Kamalakkannan, S. Prabha and S. Senthilvelan, *Mater. Res. Bull.*, **48**, 3707 (2013); https://doi.org/10.1016/j.materresbull.2013.05.121
10. J. Kazmi, P.C. Ooi, B.T. Goh, M.K. Lee, M.F.M. Razip Wee, S.S.A. Karim, S.R.A. Raza and M.A. Mohamed, *RSC Adv.*, **10**, 23297 (2020); https://doi.org/10.1039/D0RA03816D
11. O.M. Ntwaeaborwa, S.J. Mofokeng, V. Kumar and R.E. Kroon, *Spectrochim. Acta A Mol. Biomol. Spectrosc.*, **182**, 42 (2017); https://doi.org/10.1016/j.saa.2017.03.067
12. A.D. Sontakke, A. Tarafder, K. Biswas and K. Annapurna, *Physica B*, **404**, 3525 (2009); https://doi.org/10.1016/j.physb.2009.05.053
13. T. Yaba, R. Wangkhem and N.S. Singh, *J. Alloys Compd.*, **843**, 156022 (2020); https://doi.org/10.1016/j.jallcom.2020.156022
14. M. Singh, W.U. Haq, S. Bishnoi, B.P. Singh, S. Arya, A. Khosla and V. Gupta, *Mater. Technol.*, **37**, 1051 (2022); https://doi.org/10.1080/10667857.2021.1918866
15. F. Sordello, I. Berruti, C. Gionco, M.C. Paganini, P. Calza and C. Minero, *Appl. Catal. B*, **245**, 159 (2019); https://doi.org/10.1016/j.apcatb.2018.12.053
16. M. Kumar, G. Singh and M.S. Chauhan, *Ceram. Int.*, **47**, 17023 (2021); https://doi.org/10.1016/j.ceramint.2021.03.008
17. L. Cao, L. Wang, L. Xu, Y. Shen, M. Xie and H. Hao, *RSC Adv.*, **11**, 29416 (2021); https://doi.org/10.1039/D1RA05317E
18. K. Qi, X. Xing, A. Zada, M. Li, Q. Wang, S. Liu, H. Lin and G. Wang, *Ceram. Int.*, **46**, 1494 (2020); https://doi.org/10.1016/j.ceramint.2019.09.116
19. S.S. Turkyilmaz, N. Guy and M. Ozacar, *J. Photochem. Photobiol. Chem.*, **341**, 39 (2017); https://doi.org/10.1016/j.jphotochem.2017.03.027
20. K. Kasirajan, L. Bruno Chandrasekar, S. Maheswari, M. Karunakaran and P.S. Sundaram, *Opt. Mater.*, **121**, 111554 (2021); https://doi.org/10.1016/j.optmat.2021.111554
21. P. Du, L.K. Bharat and J.S. Yu, *J. Alloys Compd.*, **633**, 37 (2015); https://doi.org/10.1016/j.jallcom.2015.01.287
22. P. Yu, L. Su and J. Xu, *Opt. Rev.*, **21**, 455 (2014); https://doi.org/10.1007/s10043-014-0070-5
23. J. Huang, C. Dong, P. Huang, W. Zhong, Y. Luo, J. Li, Y. Hu, W. Duan, L. Qiu, W. Qin and Y. Xie, *Nanomaterials*, **15**, 1444 (2025); https://doi.org/10.3390/nano15181444
24. Y. Zong, Z. Li, X. Wang, J. Ma and Y. Men, *Ceram. Int.*, **40**, 10375 (2014); https://doi.org/10.1016/j.ceramint.2014.02.123
25. G.L. Bhagyalekshmi, A.P.N. Sha and D.N. Rajendran, *J. Mater. Sci. Mater. Electron.*, **30**, 10673 (2019); https://doi.org/10.1007/s10854-019-01413-x
26. A.T. Ravichandran, R. Karthick, K. Ravichandran, D. Ravinder and R. Chandramohan, *J. Mater. Sci. Mater. Electron.*, **29**, 2784 (2018); https://doi.org/10.1007/s10854-017-8206-6
27. J. Sirajudeen and J. Naveena, *Mater. Today Proc.*, **4**, 11837 (2017); https://doi.org/10.1016/j.matpr.2017.09.102
28. A.L. Al-Otaibi, E. Howsawi and T. Ghrib, *Nano-Struct. Nano-Objects*, **24**, 100551 (2020); https://doi.org/10.1016/j.nanoso.2020.100551
29. E. Chingangbam, N. Yaiphaba and G. Phaomei, *Asian J. Chem.*, **34**, 2969 (2022); https://doi.org/10.14233/ajchem.2022.23940
30. S. Mngadi, M. Singh and S. Mokhosi, *J. Polym. Eng.*, **41**, 597 (2021); https://doi.org/10.1515/polyeng-2020-0271

31. M.C. Sekhar, U. Chalapthi, V.K. Madhu Smitha, P.T. Poojitha, S. Uthanna and B. Poornaprakash, *J. Supercond. Nov. Magn.*, **30**, 1937 (2017); https://doi.org/10.1007/s10948-017-3992-x
32. H.S. Alanazi, N. Ahmad and F.A. Alharthi, *RSC Adv.*, **11**, 10194 (2021); https://doi.org/10.1039/D0RA10698D
33. V. Kumar, S. Som, V. Kumar, V. Kumar, O.M. Ntwaeaborwa and H.C. Swart, *Chem. Eng. J.*, **255**, 541 (2014); https://doi.org/10.1016/j.cej.2014.06.027
34. T.D. Thien, H. Van Thanh, L.T.M. Cham, P.D. Thang, N. Van Thang, D. Van Pham, M.H. Pham, H.N. Nhat, V. Van Hiep and N.D. Lam, *Heliyon*, **11**, e43029 (2025); https://doi.org/10.1016/j.heliyon.2025.e43029
35. A. Janotti and C.G. Van de Walle, *Rep. Prog. Phys.*, **72**, 126501 (2009); https://doi.org/10.1088/0034-4885/72/12/126501
36. G. Barsisa, A. Belay, G. Beyene, C. Seboka and K. Gudishe, *Nano Biomed. Eng.*, **14**, 58 (2022); https://doi.org/10.5101/nbe.v14i1.p58-70
37. B.P. Maheshwari, *RSC Adv.*, **4**, 32605 (2014); https://doi.org/10.1039/c4ra05903d
38. T.T.T. Huong, N.T. Sa, N.T.M. Thuy, P.V. Hao, N.H. Thao, N.T. Hien and N.X. Ca, *Nanoscale Adv.*, **7**, 909 (2025); https://doi.org/10.1039/D4NA00858H
39. V. Mangalam and K. Pita, *Materials*, **10**, 930 (2017); https://doi.org/10.3390/ma10080930
40. K.M. Girish, S.C. Prashantha, R. Naik, H. Nagabhushana and K.S. Anantharaju, *SN Appl. Sci.*, **1**, 926 (2019); https://doi.org/10.1007/s42452-019-0948-8
41. D.C. Look, K.D. Leedy, L. Vines, B.G. Svensson, A. Zubiaga, F. Tuomisto, D.R. Doutt and L.J. Brillson, *Phys. Rev. B Condens. Matter Mater. Phys.*, **84**, 115202 (2011); https://doi.org/10.1103/PhysRevB.84.115202
42. Z. Xia, Q. Xue, K. Zhang, H. Zhang and T. He, *J. Mater. Sci. Mater. Electron.*, **26**, 8078 (2015); https://doi.org/10.1007/s10854-015-3465-6
43. T. Matsunaga, S. Takeshita and T. Isobe, *J. Lumin.*, **165**, 62 (2015); https://doi.org/10.1016/j.jlumin.2015.04.011
44. J.W. Stouwdam and F.C.J.M. van Veggel, *Nano Lett.*, **2**, 733 (2002); https://doi.org/10.1021/nl025562q
45. L.A. Ramolise, S.N. Ogugua, R. Makole, E. Coetsee-Hugo, H.C. Swart and D.E. Motaung, *Opt. Mater.*, **167**, 117303 (2025); https://doi.org/10.1016/j.optmat.2025.117303
46. M.K. Hossain, M.M. Hossain, S. Akhtar and A.A. Bd, *React. Kinet. Mech. Catal.*, **135**, 2247 (2022); https://doi.org/10.1007/s11144-022-02244-4
47. K.A. Sultana, M.T. Islam, J.A. Silva, R.S. Turley, J.A. Hernandez-Viezcas, J.L. Gardea-Torresdey and J.C. Noveron, *J. Mol. Liq.*, **307**, 112931 (2020); https://doi.org/10.1016/j.molliq.2020.112931
48. I.O. Ali, H. Nady, M.I. Mohamed and T.M. Salama, *J. Indian Chem. Soc.*, **101**, 101480 (2024); https://doi.org/10.1016/j.jics.2024.101480
49. M. Farag, S.M. El-Dafrawy and S.M. Hassan, *J. Inorg. Organomet. Polym. Mater.*, **34**, 930 (2024); https://doi.org/10.1007/s10904-023-02811-9
50. S. Ben Ameur, H. BelHadjltaief, B. Duponchel, G. Leroy, M. Amlouk, H. Guermazi and S. Guermazi,, *Heliyon*, **5**, e01912 (2019); https://doi.org/10.1016/j.heliyon.2019.e01912
51. J. Puneetha, N. Kottam and A. Rathna, *Inorg. Chem. Commun.*, **125**, 108460 (2021); https://doi.org/10.1016/j.inoche.2021.108460
52. A.H. Bhat, N.A. Chopan and H.T.N. Chisti, *Nanotechnology*, **34**, 495604 (2023); https://doi.org/10.1088/1361-6528/acf6c4